INTERNATIONAL SOCIETY FOR SOIL MECHANICS AND GEOTECHNICAL ENGINEERING

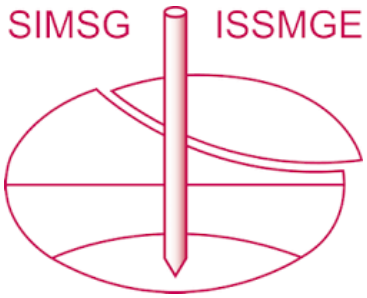

This paper was downloaded from the Online Library of the International Society for Soil Mechanics and Geotechnical Engineering (ISSMGE). The library is available here:

https://www.issmge.org/publications/online-library

This is an open-access database that archives thousands of papers published under the Auspices of the ISSMGE.

The paper was published in the proceedings of the 11th International Conference on Physical Modelling in Geotechnics (ICPMG2026) and was edited by Ioannis Anastasopoulos. The conference was held from June 8th to June 12th 2026 in Zurich, Switzerland.

ICPMG 2026

Proceedings of the 11th ICPMG 2026
11th International Conference on Physical Modelling in Geotechnics
8-12 June 2026, Zurich, Switzerland
© 2026 the Authors

Understanding Soft Soil Stability Challenges in Dutch Railways through Centrifuge Modelling

C. Cengiz
Deltares, Delft, the Netherlands, cihan.cengiz@deltares.nl

C. Zwanenburg
Deltares, Delft, the Netherlands, cor.zwanenburg@deltares.nl

T. Schweckendiek
Deltares, Delft, the Netherlands, timo.schweckendiek@deltares.nl

A.V. van Uitert
ProRail, Utrecht, the Netherlands, agnes.vanuitert@prorail.nl

ABSTRACT: This paper presents the experimental design and rationale behind the Reliable Embankments for Safe Expansion in Rail Traffic (RESET) centrifuge test series, conducted at Deltares to investigate embankment stability under controlled strength and stiffness contrast. The tests are part of a broader research program between ProRail, TU Delft, and Deltares, aimed at improving geotechnical stability assessments for railway infrastructure. Using a scaling factor of 1:50 and centrifugal acceleration of 50g, physical models of a representative Dutch railway embankment were tested to failure under displacement-controlled loading conditions. Key variables include subsoil stiffness, loading rate, embankment height, and presence of a trackside ditch. Kaolin clay was used for subsoil consistency, while failure mechanisms are captured via high-resolution imaging and sensor arrays. Preliminary observations confirm sensitivity of the failure load to stiffness contrast. The results provide a benchmark dataset for validating FEM predictions and advancing numerical models (both finite elements and limit equilibrium) for serviceability-based design.

1 INTRODUCTION

The Dutch rail network is extensive and serves 1.1 million people daily (NS, 2023). Additionally, besides the trips generated by commuters, the freight operations also rely heavily on the Dutch network (Tare et al., 2024). Given the widespread presence of soft, compressible soils in the Netherlands, network stability is a critical issue, especially for extensions of rail traffic in terms of train loads, frequency and speed. The importance of this issue is compounded by the fact that the Dutch network consists of 3000 km of embankments and 7000 km of track.

The Reliable Embankments for Safe Expansion in Rail Traffic (RESET) program aims to establish and validate strain-dependent methods for assessing embankment stability and serviceability on soft ground. Within this context, the experiment employs 1:50 scale physical models at 50 g to reproduce prototype stress levels and to observe failure mechanisms under displacement-controlled loading until collapse. The program targets three principal influences on stability, namely subsoil stiffness contrast, loading rate, and trackside ditch presence, with a dedicated variant that includes no trackside ditch to examine effects on the failure mechanism. High-resolution imaging and a dense sensor layout record the response, pore pressure evolution, and deformation fields, which enables consistent derivation of stiffness-degradation and deformation metrics. The resulting dataset is designed for calibration and validation of finite-element and limit-equilibrium approaches that incorporate strain dependency and failure.

The present paper sets out the experimental rationale and configuration, summarizes the test matrix and measurement strategy, and reports initial observations that demonstrate the sensitivity of failure load and deformation mode to the stiffness contrast between the sand embankment and the soft soil foundation. Specifically, the present contribution delves into a subset of the completed tests where the subsoil stiffness was solely varied to observe the failure loads.

The stability of railway embankments has been extensively investigated in the existing literature and

the account below is a concise reflection on the body of available research and by no means an exhaustive survey. Karstunen and Yin (2010) report the Murro test embankment on soft natural clay and show that anisotropy, bonding, and time-dependent behavior govern stability and long-term settlements. Similarly, Lehtonen et al. (2015) describe a full-scale embankment failure test at Perniö with extensive instrumentation; the failure developed by undrained creep under sustained loading, which is relevant for soft clay foundations. In this doctoral dissertation, Mansikkamäki (2015) presents effective-stress finite-element stability analyses of an old railway embankment on soft clay and highlights the importance of appropriate constitutive modelling and pore-pressure treatment. Indraratna et al. (2021) introduce a large-scale track testing facility for heavy haul conditions and quantify ballast deformation and degradation under realistic loading histories. Against this background, centrifuge modelling at 50g allows prototype-level stresses and drainage so that failure modes and stiffness-contrast effects can be observed directly under failure conditions. The present paper reports a subset of the eight-test RESET program focused on varying subsoil stiffness and provides benchmark data for finite-element (FE) and limit-equilibrium calibration on Dutch soft clays. The wider experimental campaign also investigated the loading rate effects, embankment behavior without a ditch, failure behavior with varying embankment height, and benchmark tests to assess the repeatability of the results.

2 EXPERIMENTAL METHOD

2.1 Setup and Materials

The experiments aimed at modelling a typical embankment within the national rail network of the Netherlands. The chosen embankment height in prototype scale was 2.5 m with a side-slope of 2 in 3. A clay layer thickness of 6 m was foreseen below the embankment based on the prevailing local geology of the Dutch deltas. Finite element models were run to investigate the depth of the failure planes passing through the clay to investigate the adequacy of the selected clay depth. The numerical models showed that the maximum depth of the failure plane did not extend beyond the mid-depth of the selected clay thickness. Besides the clay depth selection, additional numerical modelling was carried out to investigate the effects of the left-hand-side boundary effects. The physical models are designed to model a plane-strain half embankment as depicted in Figure 1. Therefore the proximity of the loading plate to the lateral boundary was investigated. Based on the numerical models, a 4.5 m spacing was allowed in prototype scale. The geometric specifications of the centrifuge model is outlined in Table 1.

The strongbox that houses the model is 872 mm long, 200 mm wide, and 450 mm deep (Zwanenburg et al., 2024; Cengiz et al., 2024). In order to facilitate basal drainage, a 50 mm sand layer is placed below the clay layer before the clay slurry consolidation within the strongbox. The basal sand layer is made up of Baskarp B25 sand (e_{min}= 0.35; e_{max}= 0.451 ; ϕ'_{cs} = 32). The clay used is a commercially available speswhite kaolin with a liquid and plastic limit of 66 and 27 %, respectively. The specific gravity of the material is 2.63. In the present study, three different clay stiffnesses are targeted by varying the consolidation pressure. The SHANSEP (Stress History and Normalized Soil Engineering Properties)

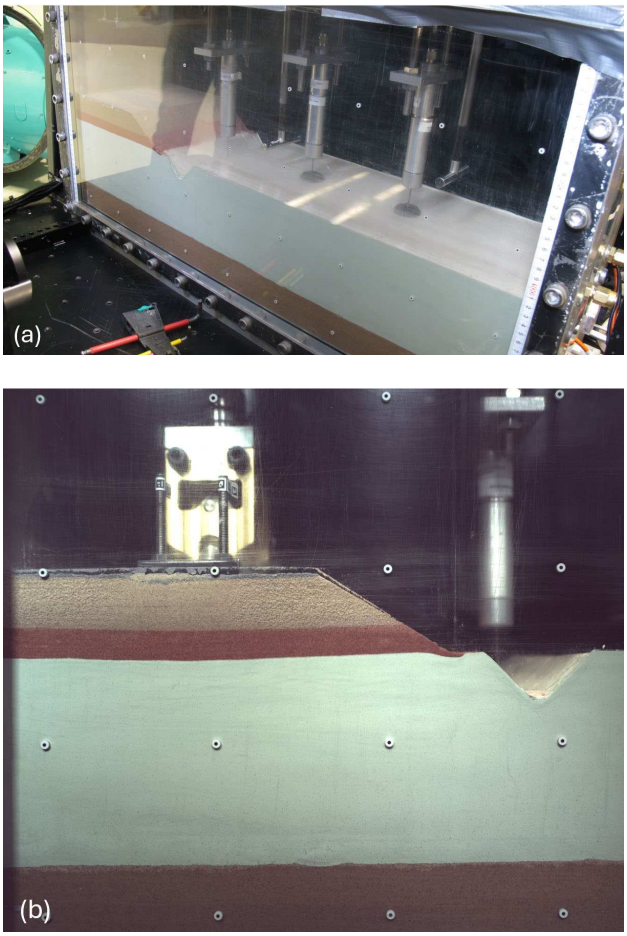

Figure 1, (a) general view of the model and (b) photograph of the model taken in-flight through the on-board centrifuge camera

parameters of the clay used are known to be S_u^{NC} = 0.19 and m = 0.805. Based on these parameters three consolidation pressures are selected which are 64,

105, 210 kPa. For Speswhite kaolin, the one-dimensional coefficient of consolidation (c_v) is on the order of $1.5 \times 10^{-7} m^2/s$

Following the consolidation of the clay to the desired overburden pressure, the embankment is constructed by way of wet pluviation and continuous tamping. The embankment body is constructed using Baskarp B15 (e_{min}= 0.36; e_{max}=0.48 ; ϕ'_{cs} = 34) sand (Cengiz et al., 2024). The volume of the embankment was scanned with a 3D scanner before and after the placement of the embankment. By making use of the mass of sand consumed by the embankment, the relative density of the embankment is calculated. The model was also scanned with and without the embankment post-failure.

The front glass of the strongbox is smeared with a clay-speckle mixture to enable the PIV analysis within the clay layer (in addition to the embankment). Besides the suite of sensors onboard the model, the clay material is also profiled with in flight T-bars. A total of two T-bar tests are performed in each test post-embankment failure. The rate of T-bar testing is set at 1 mm/s and it is consistent with the available literature on the strength profiling conducted on soft clays (White et al., 2010). The setup is heavily instrumented with a total of 19 pore water pressure gauges, 7 total pressure sensors, 3 settlement probes, and a instrumented loading plate capable of measuring loading, tilt, and settlement. A detailed sketch of the instrumentation and measurement setup is provided in Figure 2.

Table 1. Geometric and scaling properties of the model

Property	Prototype	Model
Centrifugal Acceleration (g)	1	50
Height of the embank. (mm)	2500	50
Slope of the embank. (-)	2/3	2/3
Width of ballast, one track (mm)	3000	60
Distance lat. bound. (mm)	4500	90
Distance crest and ballast (mm)	2000	40
Basal width of embankment (mm)	13250	265
Height of clay subsoil (mm)	6000	120
Ditch distance from toe (mm)	1000	20
Ditch Depth (mm)	1500	30
Ditch width (mm)	2500	50
Slope of the ditch (-)	1/1	1/1

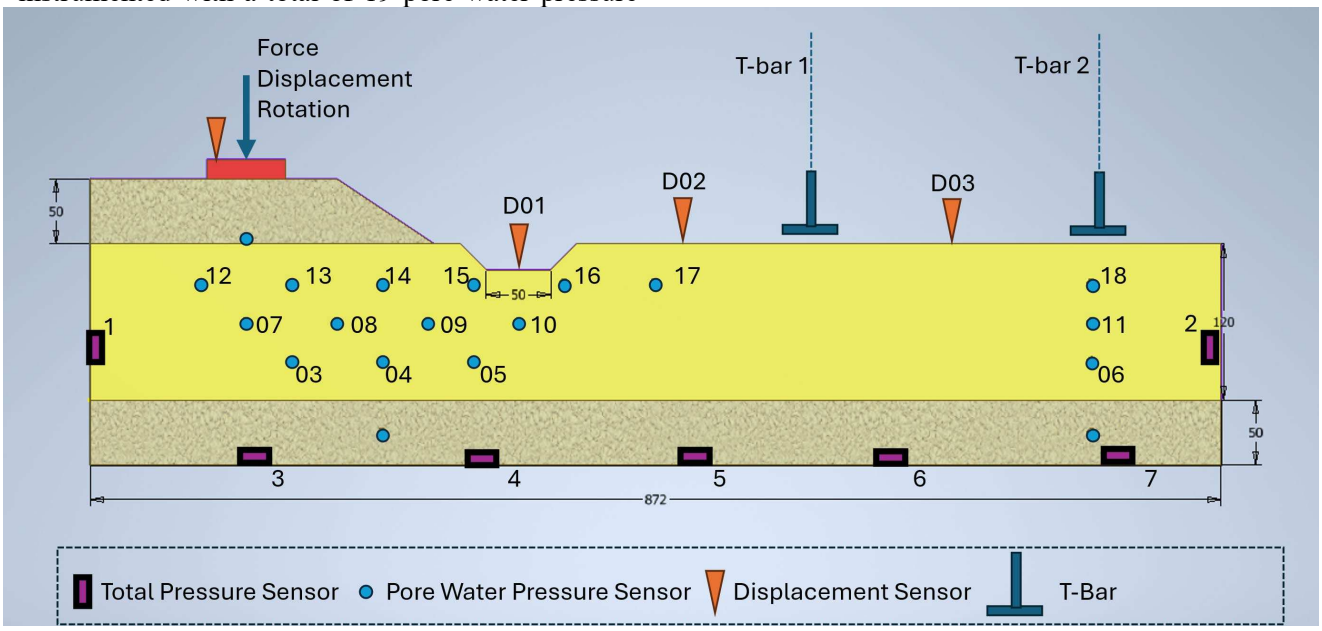

Figure 2. Instrumentation and measurement layout of the centrifuge tests.

2.2 Execution of the Tests

The embankments are brought to failure by way of displacement controlled loading which is applied at a rate of 0.2 mm/s. The loading plate (60 mm × 195 mm) is designed to operate in two modes. In the initial, rotation-restrained mode, a guide pin locks the plate to seat it on the embankment and establish a repeatable reference. At the start of loading, the pin is disengaged and the plate enters the rotation-enabled mode (up to 30°), so vertical displacement is imposed while the plate can tilt as the embankment deforms; load is transmitted via the rotation pin to the inline load cell. The rotation of the loading plate is measured by two spring-tensioned wire displacement sensors. The rotation is determined trigonometrically from the difference in the wire transducer readings. The

centrifugal acceleration regime was decided upon by way of finite elements runs. As a result of the numerical calculations, the centrifuge was ramped from 1g to 25g at 0.25 g/min, then held at 25g for 60 minutes to allow consolidation. The next increment from 25 g to 50 g took a further 100 minutes at 0.25 g/min. The 50 g level was held for 60 minutes before commencing the embankment loading at 50 g. A uniform centrifugal acceleration regime is applied in all tests and an exemplar curve representing the g-level during the test is illustrated in Figure 3. The targeted acceleration level was at the base of the embankment and the plot in Figure 3 shows the acceleration at the basket of the centrifuge hence the slight increase in the g-level.

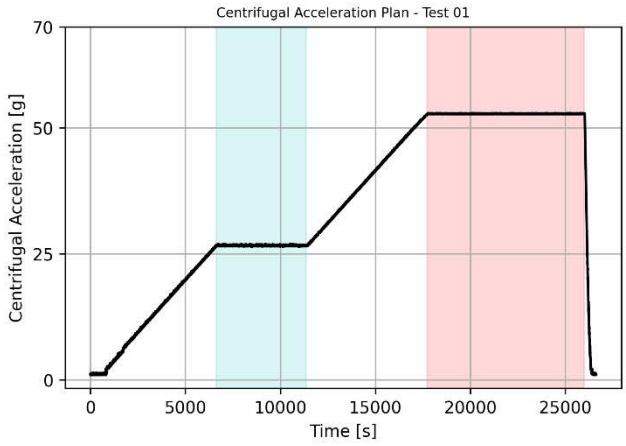

Figure 3. Centrifugal acceleration regime applied in all tests

2.3 Particle Image Velocimetry Analysis

The particle image velocimetry (PIV) analysis utilized the MATLAB-based GeoPIV-RG code (Stanier et al., 2016). The sand and clay zones are analyzed separately due to the differences in their seeding and contrast. Both sand and clay zones are discretized into 650 subsets. During the displacement controlled loading of the embankment, image capture occurred at a rate of 2 frames per second meaning that per each 0.1 mm of deformation, a high-resolution image was acquired. Figure 4 illustrates the sand and clay zone subsets (or the analysis mesh) which is 50 by 50 pixels for sand and 120 by 120 pixels for clay.

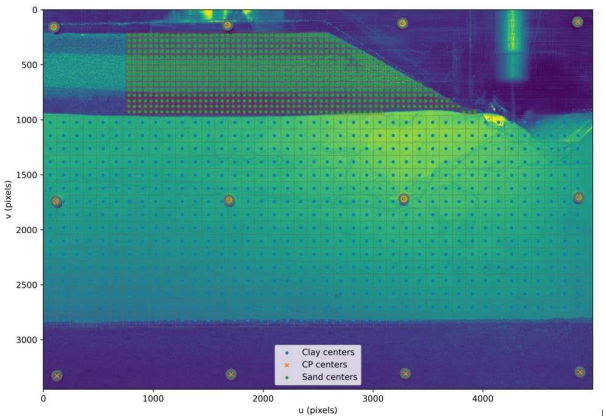

Figure 4. Subset layout for the sand embankment and clay foundation; mesh generated in GeoPIV-RG and post-processed in Python (Matplotlib).

3 RESULTS

3.1 Clay Stiffness

The T-bar used had a length of 75 mm and its diameter was 12 mm. Based on these dimensions, the L/D is about 6.25. The projected area of the T-bar is 900 mm^2 (or $9 \times 10^{-4}\ m^2$). With the 1 mm/s advancement rate, the loading is deemed to be undrained and therefore an N_{kT} value of 10.5, White et al. (2010), is selected. With the above assumptions and explanations, the first order undrained shear strength (without any corrections) is calculated as:

$$s_u = \frac{q_{net}}{N_{kT}} \quad (1)$$

where:

- s_u = first-order undrained shear strength (kPa),
- q_{net} = measured net unit resistance (kN/m²), calculated as the measured vertical force divided by the projected area of the T-bar,
- N_{kT} = bearing capacity factor for the T-bar (dimensionless), taken here as 10.5

Figure 5 illustrates the T-bar results for the considered tests. A total of two T-bar measurements were made for each test. The targeted values of undrained shear strength for the so-called soft, medium, and stiff clays were 12, 20, and 40 kPa, respectively. Due to consolidation issues within a long aspect ratio strongbox with a planar area of 872 mm by 200 mm, the resulting clay strengths deviated from the expected values.

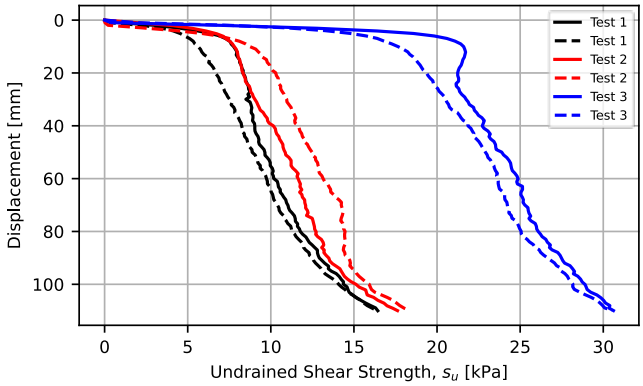

Figure 5. T-bar values of the considered tests

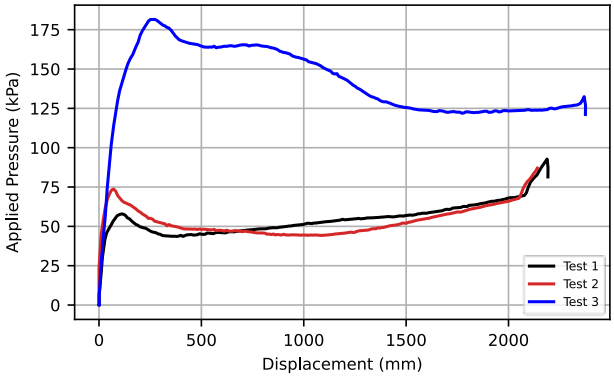

Figure 6. Applied pressure versus prototype scale displacements.

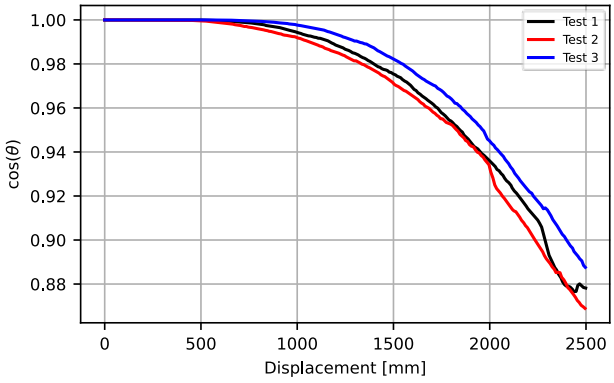

Figure 7. Plots of cosine of loading plate angle during loading for the selected tests

3.2 Embankment Failure Load

Figure 6 illustrates embankment failure loads as a function of the prototype scale displacements. The early peak resistances measured in Test 1, 2, and 3 are 57.9, 73.7, and 181.5 kPa, respectively. It is seen that the initial stiffnesses of the pressure-displacement curves are very similar. The peak load is reached in Test 3 remarkably later than the remaining tests meaning that more deformations were required to mobilize the peak resistance when the founding clay layer was stiffer. It should be noted that the large deformation curve presented herein does not reflect the serviceability or the ultimate limit state conditions from the perspective of an asset owner. It is readily known that the rail infrastructure is vulnerable to even minute levels of settlement and it is more than likely that the line would be closed for rail operations at the early parts of the curves depicted in Figure 6. For instance, Argyroudis and Kaynia (2015) define the extensive damage state for rail infrastructure at a mean permanent ground displacement of 200 mm.

The plate rotations during the embankment loading are illustrated in Figure 7. These plots show that the variation in the measured resistance is not affected by the tilt angle of the loading plate as it is seen that up to a displacement of 500 mm, no appreciable load plate tilt occurs. The PIV analysis of the tests also indicate that the dominant failure mode in the embankment is punching failure. This is confirmed by observing the deformation at the time of peak embankment bearing pressure. Nnote that this peak is in the early part of the presented curves and not the peaks observed in the tail ends of the curves which are explained by large deformations and geometric nonlinearities.

3.3 Stress-State in the Clay: Pore Water and Total Pressures

The evolution of pore water pressure (PWP) during the loading stages provides valuable insight into the stress redistribution within the clay layer and the influence of subsoil stiffness on drainage and undrained response. Figures 8–10 show the zero-corrected pore water pressure (PWP) development for the three tests corresponding to the soft, medium, and stiff clay conditions. The sensor readings are zeroed at the beginning of the prescribed displacement application. The sensors in these plots are selected based on their 'activity' which means that the overall change in the readings during the loading period was greater than 3 kPa.

In Tests 1 and 2, the excess pore water pressures increase markedly with displacement, reaching up to 40 kPa at a displacement level of 500 mm. This trend reflects a strongly contractive behavior in the softer foundations, where shear deformation induces substantial excess pressures and reduces effective stress. In contrast, the stiff clay in Test 3 exhibits a higher PWP response on average however, the magnitude of measured water pressures seems to

decrease steadily as the loading is progressed. This indicates that the imposed deformation is largely accommodated through shear without significant pore-pressure generation at large deformation.

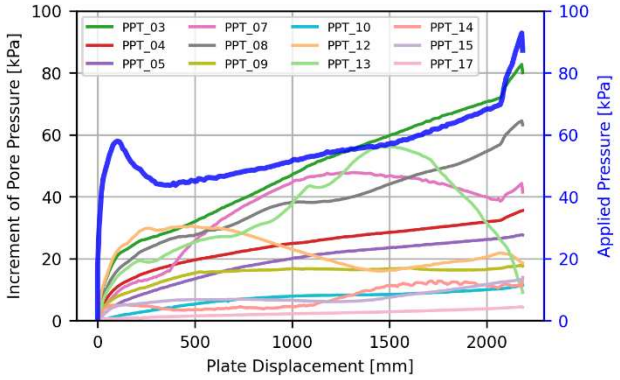

Figure 8. Evolution of PWPs during Test 1 (notice that the PWP values are zeroed at the beginning of the prescribed displacement application)

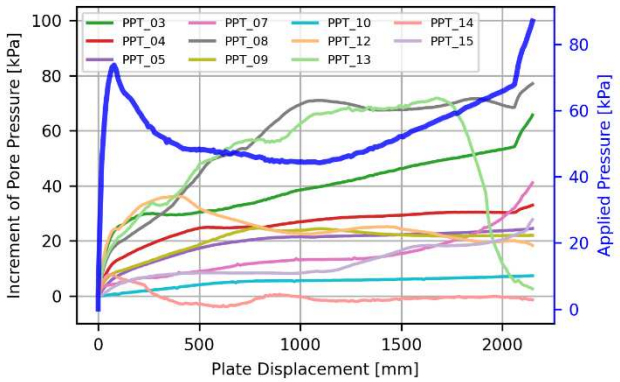

Figure 9. Evolution of PWPs during Test 2 (notice that the PWP values are zeroed)

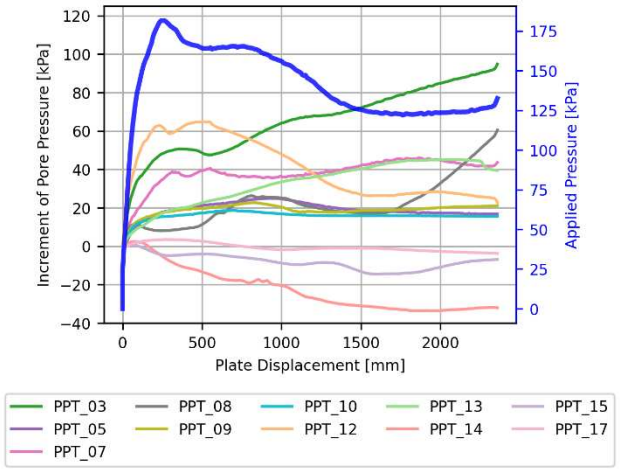

Figure 10. Evolution of PWPs during Test 3 (notice that the PWP values are zeroed)

The evolution of pore water pressure (PWP) provides clear evidence of the contrasting hydraulic and mechanical responses of the clay subsoil across the three tests. As shown in Figure 11, the average PWP increases steadily with displacement in the softer foundations (Tests 1 and 2), indicating a contractive response and progressive buildup of excess pore pressures under loading. In contrast, the stiff clay (Test 3) exhibits a markedly different trend where the initial PWP is substantially higher than in the softer cases, yet its subsequent rise is limited, followed by a gradual reduction as loading progresses.

This behavior is further emphasized in Figure 12, which presents the average change in PWP relative to the start of loading. The softer clays show a continuous increase in ΔPWP with displacement, reflecting the accumulation of undrained excess pressures and loss of effective stress. Conversely, the stiff clay shows only a minor net increase, despite its lower permeability.

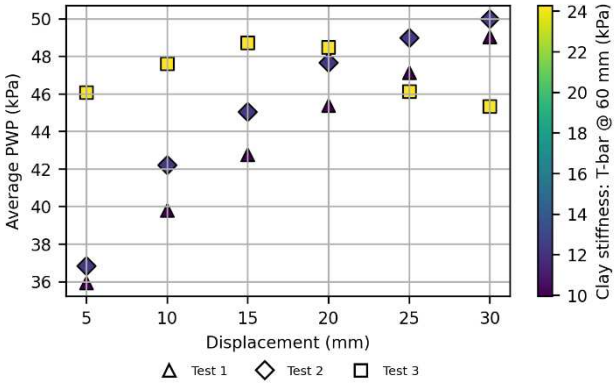

Figure 11. Average pore water pressure (PWP) evolution with displacement for the three tests

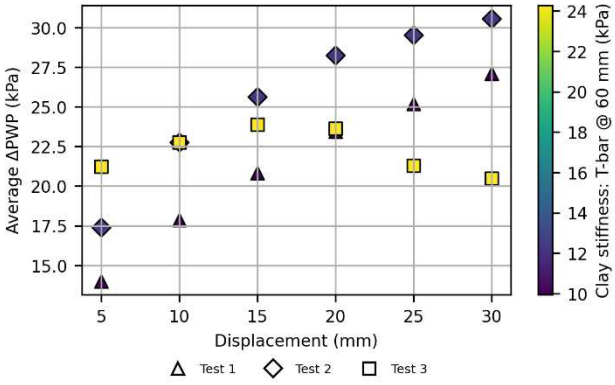

Figure 12. Average change in pore water pressure (ΔPWP) with displacement

Figure 13 illustrates the measured lateral soil pressure at the left-hand-side boundary of the model (please refer to Figure 2). As expected, the peak load imposed on the lateral boundary increases with increasing clay stiffness. Similar trends are also seen for the total pressure gauges placed at the base of the assembly as depicted in Figure 14 and Figure 15. While the trend

observed in Figure 14 is consistent with the general trends of lateral pressure increase, the continual increase of the measured pressure in Figure 15 can be interpreted as the added surcharge load due to shifting of clay over to the sensor at large displacement. Further insights can be derived from the ratio of the lateral pressure to the applied embankment loading as depicted in Figure 16.

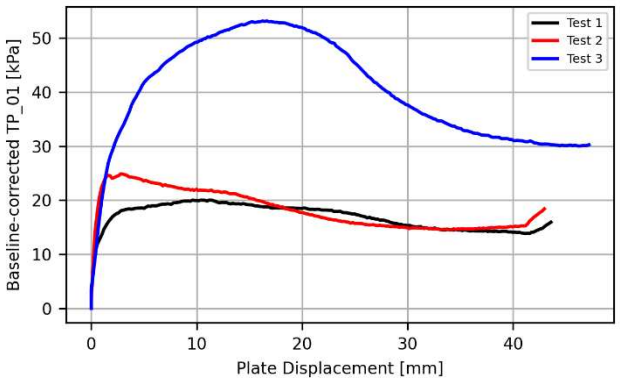

Figure 13. Plots of the measured lateral stress at the left-hand-side boundary as a function of the applied plate displacement

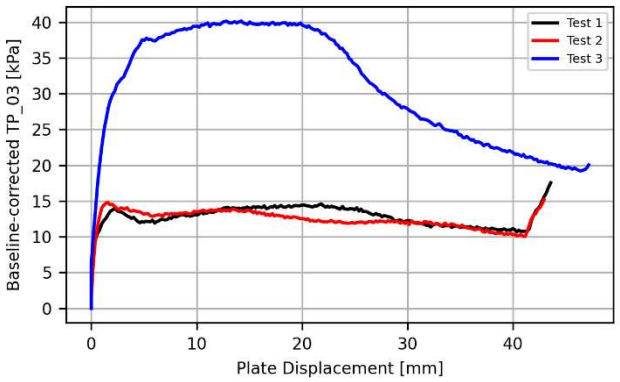

Figure 14. Plots of the measured lateral stress at the bottom boundary (directly under the embankment) as a function of the applied plate displacement

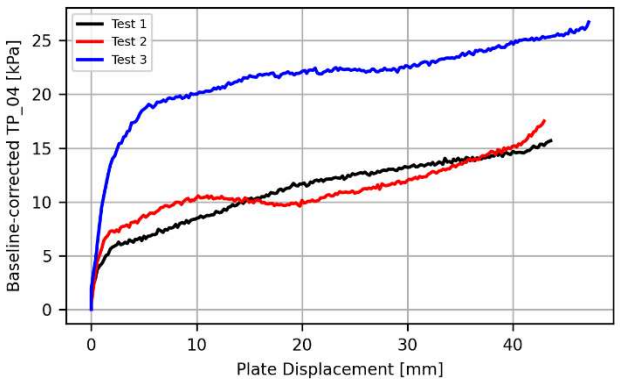

Figure 15. Plots of the measured lateral stress at the bottom boundary (under the ditch) as a function of the applied plate displacement

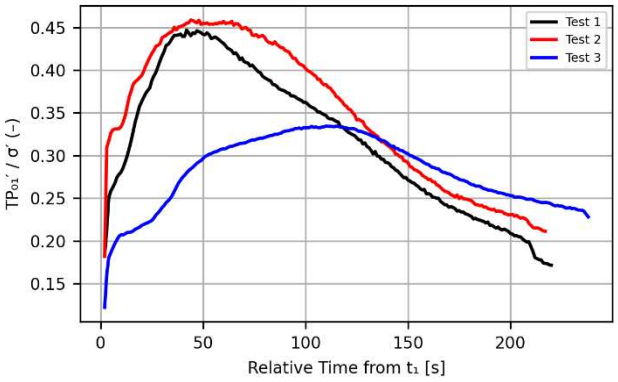

Figure 16. Plots of measured lateral stress normalized with applied embankment loading for all tests

3.4 PIV Analysis

At the time of drafting of this contribution, the PIV analysis was still on-going. Therefore, a limited view on the deformation field is provided in what follows. The peak embankment load was mobilized at model scale displacements of, 2.07, 1.56, and 5.05 mm, which correspond to 103.5, 78, and 252.5 mm in prototype-scale. In all tests, the deformation field in the sand embankment was confined to a small shear/smear zone as can be seen in the displacement field plots depicted in Figure 17, Figure 18, and Figure 19 for Tests 1, 2, and 3, respectively.

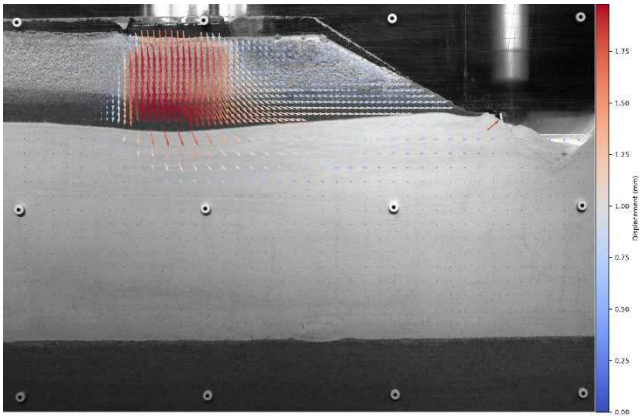

Figure 17. A snapshot of the displacement field in Test 1 at the time of peak embankment loading

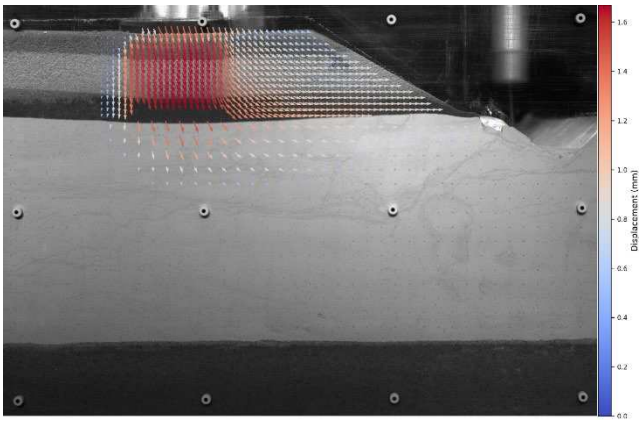

Figure 18. A snapshot of the displacement field in Test 2 at the time of peak embankment loading

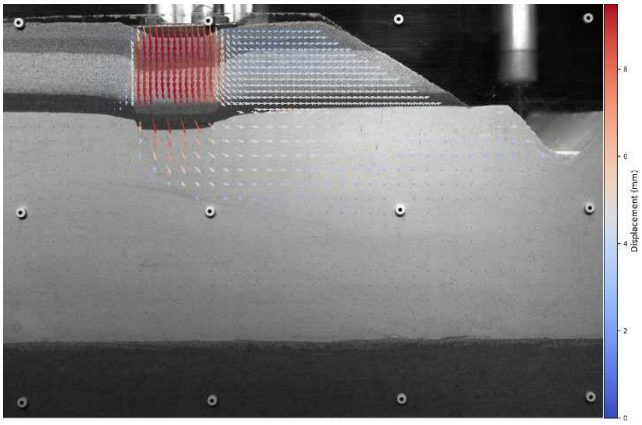

Figure 19. A snapshot of the displacement field in Test 3 at the time of peak embankment loading

4 CONCLUSIONS

This study reported on a centrifuge campaign (at 50 g) on a plane-strain embankment over soft to stiff clays was executed with dense instrumentation (total pressure, pore pressure, settlement) and preliminary PIV. The work quantified load–displacement behavior, pore water pressure trends, total stress changes, and deformation patterns across three foundation stiffnesses. The following conclusions can be drawn from the study:

- Peak applied embankment stress increases with foundation stiffness, while the displacement needed to mobilize peak is larger in the stiff clay and smaller in the soft clays.
- In the softer foundations, excess pore-water pressures increase steadily with displacement (reaching on the order of several tens of kPa), and causing progressive reduction of effective stress. In the stiff foundation, pore pressures are higher initially but show only limited net increase and tend to reduce as loading progresses, consistent with shear being accommodated with less excess-pressure accumulation at large deformation.
- PIV analysis shows a narrow shear/smear zone within the sand embankment for all tests at the mobilization of the peak strength, consistent with a punching-dominated mechanism.

ACKNOWLEDGEMENTS

The authors would like to express their sincere gratitude to ProRail for their generous financial support of the RESET program on railway embankment stability. Their contribution made it possible to conduct the experimental investigations, data collection, and analysis that form the foundation of this study.

REFERENCES

Argyroudis, S., Kaynia, A.M., 2015. Analytical seismic fragility functions for highway and railway embankments and cuts. *Earthquake Engineering & Structural Dynamics* 44, 1863-1879.

Cengiz, C., Cabrera, M., Wittekoek, B., Fransen, M., Wopereis, L., Zwanenburg, C., 2024. Centrifuge tests on the uplift and deformation patterns of clay cover layers in deltas, *Geotechnical Engineering Challenges to Meet Current and Emerging Needs of Society*. CRC Press, pp. 1052-1055.

Indraratna, B., Ngo, T., Ferreira, F.B., Rujikiatkamjorn, C., Tucho, A., 2021. Large-scale testing facility for heavy haul track. *Transportation Geotechnics* 28, 100517.

Karstunen, M., Yin, Z.-Y., 2010. Modelling time-dependent behaviour of Murro test embankment. *Géotechnique* 60, 735-749.

Lehtonen, V., Meehan, C., Länsivaara, T., Mansikkamäki, J., 2015. Full-scale embankment failure test under simulated train loading. *Géotechnique* 65, 961-974.

Mansikkamäki, J., 2015. *Effective stress finite element stability analysis of an old railway embankment on soft clay*.

Nederlandse-Spoorwegen, 2023. *Halfjaarcijfers* NS 2023.

Stanier, S.A., Blaber, J., Take, W.A., White, D., 2016. Improved image-based deformation measurement for geotechnical applications. *Canadian Geotechnical Journal* 53, 727-739.

Tare, A., Nefs, M., Koomen, E., Verhoef, E., 2024. Spatial drivers of logistics development in the Netherlands. *Journal of Transport Geography* 121, 104047.

White, D., Gaudin, C., Boylan, N., Zhou, H., 2010. Interpretation of T-bar penetrometer tests at shallow embedment and in very soft soils. *Canadian Geotechnical Journal* 47, 218-229.

Zwanenburg, C., Cengiz, C., Fransen, M., Wittekoek, B., Wopereis, L., 2024. *Testing dike stability under uplift conditions; an experimental study*.